Linear Triangles versus Biquadratic Quadrangles in RCS computations

Alexander Herschlein, Jürgen von Hagen, Dietmar Löffler, Werner Wiesbeck
Institut für Höchstfrequenztechnik und Elektronik,
Universität Karlsruhe (TH), Kaiserstr. 12, 76133 Karlsruhe, Germany

Abstract— **The present contribution compares the geometric approximations of linear triangles and biquadratic quadrangles for Boundary Element Methods. The PMCHW formulation for electromagnetic problems is applied to three canonical problems: a flat plate, a perfect electric conducting sphere, and a sphere with a low dielectric contrast. The biquadtratic quadrangles show to yield more accurate numerical results at less meshing expense. Also, the surface elements may be larger than the ones of linear triangles.**

I. Introduction

Numerical methods that discretize the boundaries between media are summarized as Boundary Element Methods. The accuracy of the computations based on the discretized boundaries relies mainly on two conditions: first, the geometrical approximation of the curved surfaces by suitably chosen elements, and second, the mathematical approximation of the physical quantities on the curved surface. Both parts should be carefully taken into account in order to obtain fast and accurate results.

The Method of Moments [1] is one particular Boundary Element Method that uses the electric and magnetic surface current densities on interfaces between two regions as physical quantities to be computed. For the formulation on the surface, the boundary conditions for the electric fields (electric field integral equation EFIE), the magnetic fields (magnetic field integral equation MFIE), or both (the so-called PMCHW formulation, [2]) are commonly used. The comprehensive formulation of the three integral formulations is detailed in [3] and shall not be repeated here. Only the PMCHW formulation results in physically correct solutions and shows no spurious modes even for closed bodies. Also the results for dielectric bodies are more accurate compared to only EFIE or MFIE formulations [4]. Common to all integral equations is the enforcement of the boundary conditions at the interface by induced electric and/or magnetic surface currents. In general, the geometry is approximated by surface elements. The surface current basis functions are then approximating the unknown surface currents on these surface elements.

Linear triangles [5] have commonly been used in the past for the geometrical approximation. Linear triangles are able to discretize almost any arbitrary surface and, hence, offer a considerable advantage to other, purpose-designed elements. In recent publications, the need for better approximations has become apparent. Curvilinear, triangular patches have been used in addition to higher order Lagrange polynomials on metallic bodies to represent the physical currents on the surface elements [6]. Considerable advantages have been shown [6] for the higher-order elements when applied to perfect conducting bodies.

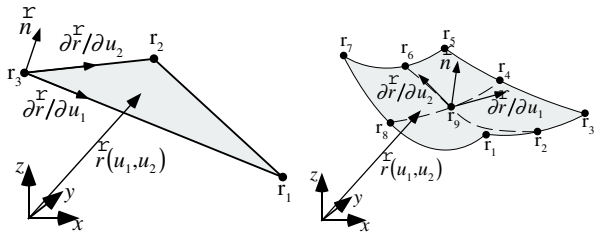

Fig. 1. Triangular (left) and biquadratic (right) surface patches for geometrical approximations.

In the present contribution, two basic shapes of surface elements are compared: the commonly used linear triangles [5] and biquadratic quadragles [3], [7], [8]. The inherent shortcomings of triangles are identified based on physical considerations for the currents on simple canonical bodies, e.g., plates and spheres. The biquadratic quadragles are shown to remedy the shortcomings while preserving the versatility of generally applicable surface elements. They are applied to the integral equations using the PMCHW formulation. The biquadratic elements result in smoother current distributions as well as physically correct current representations for scatterers with edges. The results obtained for the radar cross section of a metallic and a dielectric sphere are highly accurate even for a surface area larger than one hundredth of a squared wave length of each geometrical discretization element.

II. Geometrical Approximation of Arbitrary Shaped Surfaces

A. Triangular Approximation

Linear triangles (see Fig. 1, left) offer two advantages. First, almost any geometry can be approximated by the linear triangles [5]. Second, the mathematical description of the surface representation is relatively simple.

Any point $\vec{r}_n$ on the surface of a triangle n is parameterized by two local variables $u_1 \in [0 \ldots 1]$ and $u_2 \in [0 \ldots 1]$ by the equation

$$\vec{r}_n(u_1, u_2) = u_1 \vec{r}_{n1} + u_2 \vec{r}_{n2} + (1 - u_1 - u_2)\, \vec{r}_{n3}. \qquad (1)$$

Here, $\vec{r}_{nk}$, $k = 1, 2, 3$ are the positions of the corners of the triangle n. As the surface of the triangle is planar, the object's surface is linearly interpolated.

B. Biquadratic Approximation

For an approximation of the surface of a body by biquadratic quadrangles, the surface of each element is approximating the scatterer's surface by two Lagrange interpolations using nine sample points: the four corners and, additionally, the four points on the center of the edges, and the center point of the surface element n [3], [7], [8], [9]

$$\vec{r}_n(u_1, u_2) = \sum_{k=1}^{9} \alpha_{nk}(u_1 u_2) \,.\vec{r}_{nk} \tag{2}$$

The form functions α_{nk} are obtained by the two-dimensional Lagrange interpolation and define any point on the surface of the element n:

$$\alpha_{n1}(u_1, u_2) = \frac{1}{4} u_1 (u_1 - 1)\, u_2 (u_2 - 1) \tag{3}$$

$$\alpha_{n2}(u_1, u_2) = \frac{1}{2}\left(1 - u_1^2\right) u_2 (u_2 - 1) \tag{4}$$

$$\alpha_{n3}(u_1, u_2) = \frac{1}{4} u_1 (u_1 + 1)\, u_2 (u_2 - 1) \tag{5}$$

$$\alpha_{n4}(u_1, u_2) = \frac{1}{2} u_1 (u_1 + 1)\left(1 - u_2^2\right) \tag{6}$$

$$\alpha_{n5}(u_1, u_2) = \frac{1}{4} u_1 (u_1 + 1)\, u_2 (u_2 + 1) \tag{7}$$

$$\alpha_{n6}(u_1, u_2) = \frac{1}{2}\left(1 - u_1^2\right) u_2 (u_2 + 1) \tag{8}$$

$$\alpha_{n7}(u_1, u_2) = \frac{1}{4} u_1 (u_1 - 1)\, u_2 (u_2 + 1) \tag{9}$$

$$\alpha_{n8}(u_1, u_2) = \frac{1}{2} u_1 (u_1 - 1)\left(1 - u_2^2\right) \tag{10}$$

$$\alpha_{n9}(u_1, u_2) = \left(1 - u_1^2\right)\left(1 - u_2^2\right) \tag{11}$$

where u_1 and u_2 take values between -1 and $+1$; they constitute the local coordinate system of each surface element. The sample points on the surface of the quadrangle are defined according to Fig. 1

$$\begin{array}{lll} \vec{r}_n(-1,-1) = \vec{r}_1 & \vec{r}_n(0,-1) = \vec{r}_2 & \vec{r}_n(1,-1) = \vec{r}_3 \\ \vec{r}_n(-1,0) = \vec{r}_8 & \vec{r}_n(0,0) = \vec{r}_9 & \vec{r}_n(1,0) = \vec{r}_4 \\ \vec{r}_n(-1,1) = \vec{r}_7 & \vec{r}_n(0,1) = \vec{r}_6 & \vec{r}_n(1,1) = \vec{r}_5. \end{array}$$

As examples for the versatility of biquadratic quadrangles, Fig. 2 shows in each subfigure one single quadrangle. The corners r_1, r_3, r_5, r_7 are highlighted by black points in Fig. 1. Each quadrangle approximates closely planar surfaces (a and c), curved surfaces with one (b and d), and two curvatures (g and h). A circle or a half-sphere are already closely represented by only one element, as seen in subfigure e and f, respectively. Note that each geometrical curve is approximated only by one biquadratic quadrangle.

C. Directional Derivatives

For any surface element n, the directional derivatives are necessary for the geometrical description and the subsequent evaluation of the derivatives of the physical quantities on the surface elements [3], [7].

The directional derivatives are expressed in the local coordinates as

$$\frac{\partial \vec{r}_n(u_1, u_2)}{\partial u_1} \tag{12}$$

and

$$\frac{\partial \vec{r}_n(u_1, u_2)}{\partial u_2}. \tag{13}$$

The coefficients of the metric tensor are

$$g_{nij} = \frac{\partial \vec{r}_n(u_1, u_2)}{\partial u_i} \frac{\partial \vec{r}_n(u_1, u_2)}{\partial u_j} \tag{14}$$

with $i, j = 1, 2$ and obtained with the above directional derivatives. The determinant of the metric tensor for element n is

$$g_n = g_{n11} g_{n22} - g_{n12}^2. \tag{15}$$

The differential surface element is obtained by the differential coordinate system

$$d\vec{S}_n = \frac{\partial \vec{r}_n(u_1, u_2)}{\partial u_1} \times \frac{\partial \vec{r}_n(u_1, u_2)}{\partial u_2}. \tag{16}$$

The surface of the differential surface element is

$$dS_n = \sqrt{g_n}\, du_1\, du_2. \tag{17}$$

The normal vector of the surface element is finally defined as

$$\vec{n}_n = \frac{1}{\sqrt{g_n}} \frac{\partial \vec{r}_n(u_1, u_2)}{\partial u_1} \times \frac{\partial \vec{r}_n(u_1, u_2)}{\partial u_2}. \tag{18}$$

The divergence of a physical quantity $\vec{F}$ (later the electric or magnetic surface currents) acting in the surface is obtained by

$$\nabla_s \cdot \vec{F}_n(u_1, u_2) = \frac{1}{\sqrt{g_n}} \sum_{i=1}^{2} \frac{\partial\left(f_{u_i} \sqrt{g_n}\right)}{\partial u_i}. \tag{19}$$

Here, the f_{u_i} are the components of F in the two coordinate directions u_1 and u_2.

III. Physical Approximation of Surface Currents: Roof-Top Basis Functions

Besides the geometrical approximation of the shape of a body, also the current densities on the surface elements need to be approximated. A physical representation of the currents is compulsory, furthermore, the representation should be as close as possible to the solution. Therefore, the following requirements should be fulfilled:

- no current flow orthogonal to an outer edge
- the normal component of a current at a common edge is constant and continuous. This ensures that no line charges are generated.

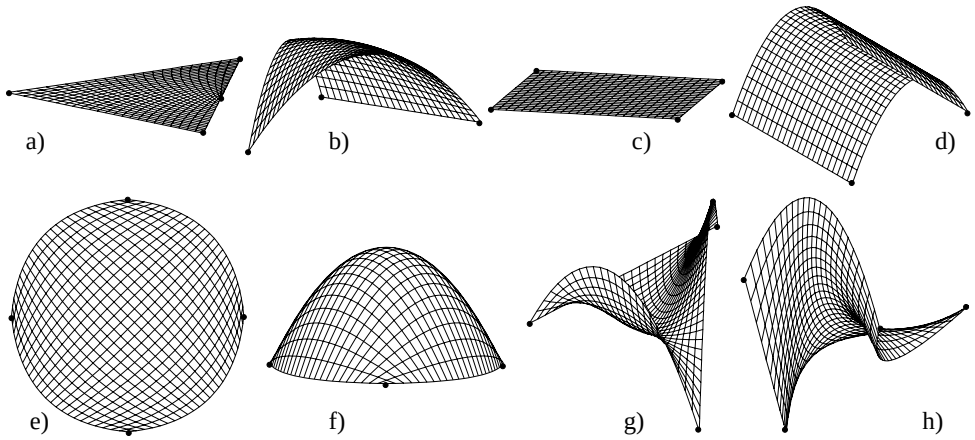

Fig. 2. One biquadratic quadrangle approximates various shapes.

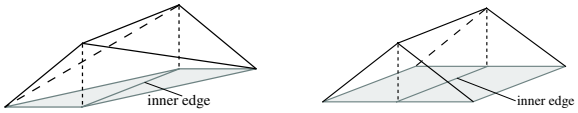

Fig. 3. Roof-top function across the common edge of two triangular (left) and rectangular (right) surface elements.

One common current representation is the Roof-Top representation which fulfills the above requirements and will be used in this contribution.

The currents on the surfaces are represented by linear functions in the local u_1, u_2-system combining the current densities on two neighboring surface elements by placing the maximum of the current orthogonal to a common edge at the position of the common edge. Thus, the currents are approximated by linear basis functions and given by the directional derivatives of the corresponding surface element n at the position $\vec{r}_n$

$$\vec{F}_n(u_1, u_2) = f_{u_1} \frac{\delta \vec{r}_n}{\delta u_1} + f_{u_2} \frac{\delta \vec{r}_n}{\delta u_2}. \tag{20}$$

Here, f_{u_1} and f_{u_2} define the shape of the basis function, in the present case roof-top functions. Roof-top functions are constant in one coordinate direction (orthogonal to the current density flow) and linear triangular in the second coordinate direction. One roof-top function in the local u_1, u_2-system is shown in Fig. 3 across the common edge of two triangular and rectangular surface elements.

In the following, only electrical surface currents are itemized, magnetic surface currents are analogous.

A. Linear Triangles and Roof-Top Basis Functions

Two linear triangles T_m^+ and T_m^- for a surface approximation are shown in Fig. 4 [5]. Their common edge is denoted m, the source positions on the triangles are $\vec{r}_m^+$ and $\vec{r}_m^-$ in the global coordinate system and $\vec{\rho}_m^+$ and $\vec{\rho}_m^-$ in the local coordinate systems. The basis function $\vec{j}_m'$ for a current

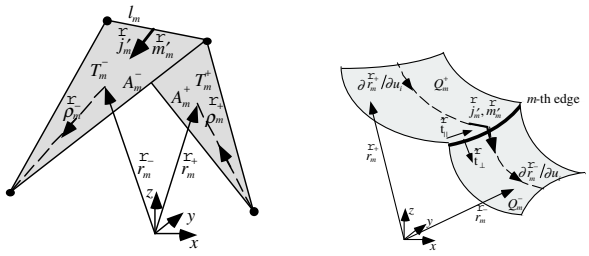

Fig. 4. Roof-Top basis functions on neighbouring surface elements: left linear triangles, and right biquadratic quadrangles.

that flows from T_m^+ to T_m^- is then

$$\vec{j}_m' = \begin{cases} \frac{l_m}{2A_m^+} \vec{\rho}_m^+ & \vec{r}_m \text{ in } T_m^+ \\ \frac{l_m}{2A_m^-} \vec{\rho}_m^- & \vec{r}_m \text{ in } T_m^- \\ 0 & \text{else.} \end{cases} \tag{21}$$

The surface divergence is

$$\nabla_S' \cdot \vec{j}_m' = \begin{cases} \frac{l_m}{A_m^+} & \vec{r}_m \text{ in } T_m^+ \\ -\frac{l_m}{A_m^-} & \vec{r}_m \text{ in } T_m^- \\ 0 & \text{else.} \end{cases} \tag{22}$$

B. Biquadratic Quadrangles and Roof-Top Functions

In Fig. 4 (right) the roof-top functions are shown for two neigbhbouring biquadratic surface elements Q_m^+ and Q_m^-. The basis functions are given for the surface current on the surface elements

$$\vec{j}_{u_1 m} = \sqrt{\frac{g_{22}(u_{1m}, u_{2m})}{g(u_1, u_2)}} T_{u1}(u_1) P_{u2}(u_2) \frac{\delta \vec{r}}{\delta u_1} \tag{23}$$

$$\vec{j}_{u_2 m} = \sqrt{\frac{g_{11}(u_{1m}, u_{2m})}{g(u_1, u_2)}} T_{u2}(u_2) P_{u1}(u_1) \frac{\delta \vec{r}}{\delta u_2}. \tag{24}$$

Here, $P_{u1,2}(u_{1,2})$ is the constant function in one dimension, $T_{u1,2}(u_{1,2})$ the triangular function in the other dimension

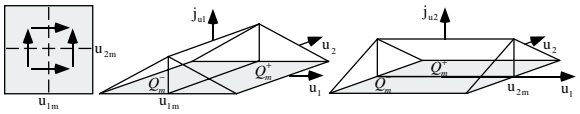

Fig. 5. Roof-Top basis functions on quadrangles in the parameter space.

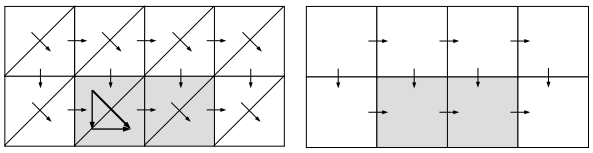

Fig. 6. Surface discretization of a rectangular plate by triangular surface elements and biquadratic rectangles.

(see Fig. 5) defined by

$$T_{u1,2}(u_{1,2}) = \begin{cases} \frac{1}{2} + \frac{1}{2}u_{1,2} & \text{for } u_{1,2m} = +1 \\ \frac{1}{2} + \frac{1}{2}u_{1,2} & \text{for } u_{1,2m} = -1 \end{cases} . \qquad (25)$$

This ensures that no normal component is present at outer edges.

C. Comparison of linear triangles and biquadratic quadrangles

Fig. 6 shows the discretization and possible currents on a rectangular plate discretized by triangular and rectangular surface elements. Gray surface elements are situated at the border of the plate being a discontinuity of the plate. The physical current normal to the border has to vanish, hence, the current must be oriented parallel to the edge.

The current on triangular functions yields two components that are oriented orthogonally and parallel to the edge, hence an unphysical surface current close to the border exists. In other words, a constant current along the border is not accessible to linear triangles. To remedy this, the biquadratic approximation accurately models a constant current parallel to an outer edge as well as the normal component.

This will be shown with the following example. Consider a flat rectangular plate with size $1.5\lambda \times 0.7\lambda$ along the x-axis and the y-axis, respectively. A plane wave at $f = 150$ MHz is incident normally with the $\vec{E}$-vector along the longer side of the plate or the x-direction.

Fig. 7 shows the x-polarized current density $\|J_x\|$, or co-polarized in the direction of the E vector. The figure on the left shows the current modeled by linear triangles, ans the figure on the right shows the the biquadratic quadrangles. Both approximations seem to model quite closely the physical current densities.

A different picture is seen for the y-polarized, or cross-polarized, surface current densities $\|J_y\|$ in Fig. 8. The differences between the results for the triangular and the biquadratic surface elements are clearly seen at the borders of the plate at $y = \pm 0.7$ m. The triangles cause a current

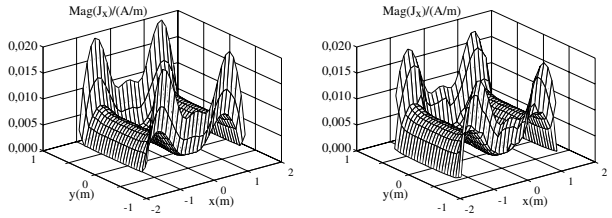

Fig. 7. x-polarized surface current densities of a rectangular plate by triangular surface elements (left) and biquadratic rectangles (right).

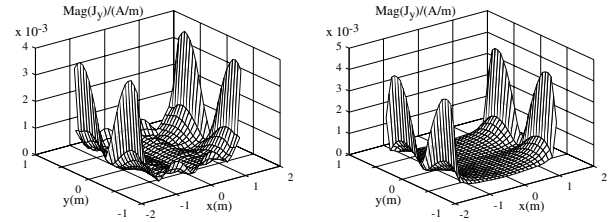

Fig. 8. y-polarized surface current densities of a rectangular plate by triangular surface elements (left) and biquadratic rectangles (right).

density orthogonal close to the edges ± 0.7 m. Even though the current magnitude only reaches approximately 25 %, these currents are nonphysical and result in a higher than physical reflection. As discussed above, the linear triangles are not able to model the correct physical current densities (see Fig. 6).

Figure 9 shows the phase of the y-polarized surface current densities (orthogonally polarized to the incident wave). The figure on the left shows the phase obtained by the linear triangular approximation. The phase exhibits large steps that are no multiple phase shifts of 360 °. The figure on the right shows the smooth phase obtained by the biquadratic quadrangles with the correct physical phase

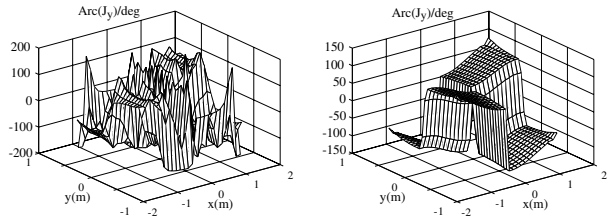

Fig. 9. Phase of the y-polarized surface current densities of a rectangular plate by triangular surface elements (left) and biquadratic rectangles (right).

TABLE I
SPURIOUS MODES AT FREQUENCY f IN MHz OF A SPHERE WITH RADIUS $r = 1$ m. MODES ARE DENOTED BY p AND n.

p / n	1	2	3	4	5	6	7
1	214	275	333	390	446	502	556
2	369	434	497	558	619	678	736
3	520	587	654	...			

behavior over the complete plate. Biquadratic quadrangles are, hence, much better suited to model edges of scatterers than linear triangles. This holds for both flat objects as well as three-dimensional objects with a non-negligible thickness.

In the following, the radar cross section of a smooth 3D scatterer is computed, and the results of different approximations will be compared.

IV. Monostatic Radar Cross Section of a Sphere

A. Canonical Problem: Sphere

The canonical shape "sphere" has been chosen to analyze the capabilities of the discretization schemes. The specific advantage of the sphere is the fact that an analytical solution exists for the radar cross section. By comparing the numerical results to the results of the Mie solution [10] a simple and accurate benchmark exists.

For the present contribution, a sphere with radius 1 m is chosen, the geometrical surface area of the sphere is hence 4π m^2. The origin of the sphere is at the origin of the spherical co-ordinate system.

Numerical solutions by the EFIE or MFIE solely are known to suffer from spurious modes. These spurious modes occur at frequencies where the interior problem (the hollow sphere) exhibits eigen modes. For the sphere with a radius of 1 m, some of the frequencies are shown in table I. At these frequencies, the solution of EFIE or MFIE methods may show erroneous results.

B. Possible Meshing Schemes

Linear triangles linearly interpolate the scatterer's surface which is modelled by flat surface elements. For an accurate surface modelling, very small discretization elements should be chosen. For comparison purposes, three different discretization schemes for linear triangles are used in the remainder.

A first discretization scheme is obtained by discretizing the sphere directly. No symmetry or any other special property of the sphere is taken into account. Two discretization levels produce two meshes, denoted by $a1$ and $a2$, with 288 and 2586 triangles and 432 and 3879 unknowns, respectively.

One possibility to improve the accuracy especially for symmetric objects as spheres is to impose a symmetric mesh for the object. For one particular incidence and a given co-ordinate system, an electric and magnetic symmetry according to the symmetry of both the object and the incident field with respect to the co-ordinate system helps to increase the accuracy. However, for a general application, electric and/or magnetic symmetries are not available as the symmetry changes with direction of incidence. In this paper, a geometrical symmetry for the object is observed, hence the mesh was modified to include this symmetry by meshing one eighth of the shpere and useing symmetry for the remaining seven eighths s of the sphere (scheme b). Again, two meshes are produced, the first (scheme $b1$) with with 352 triangles and 528 unknowns for the complete sphere, the finer mesh (scheme $b2$) with 2688 triangles and 4032 unknowns.

The third scheme follows a common way to improve results obtained by linear triangles: the surface areas of the model (e.g. the surface of all triangles) and the geometrical body are compared. Then the triangles are scaled to obtain an area that is as close as possible to the original one. This is only possible for canonical shapes as e.g. spheres, cylinders, or rectangular bodies as usually the surface of the geometrical body is not accessible to the modeller. In the present case, the two meshes $c1$ and $c2$ have 352 and 2688 triangles with 528 and 4032 unknowns, respectively.

In the case of biquadratic quadrangles, the reference points for each discretization element are chosen on the surface of the scatterer. Due to the inherent conformal shape of the discretization elements, the surface is very closely modelled. Only one mesh, scheme d, will be represented here. No attempt was made to include symmetry. This mesh uses 216 mesh elements with an average surface of $0.0582\,\mathrm{m}^2$ or $\lambda^2/69$ for each surface patch. The mesh results in 432 unknowns that represent the electric current densities on the scatterer.

The meshing schemes are summarized in Table II.

C. Angle of Incidence Sweep for PEC Sphere

At first, the monostatic radar cross section of a perfect electric conducting sphere is computed. A plane wave with $f = 150$ MHz, $\lambda = 2$m is incident, at this frequency the sphere's diametre is one wavelength. The computed frequency is well below the first eigen frequency, the EFIE computation does, hence, not suffer from any discernable contributions of a spurious mode. The analytical value of the monostatic radar cross section $RCS_{\mathrm{Mie}} = 3.7894$ dBsm is calculated by the Mie-series [10]. In all figures, the analytical value is represented by a straight line with no markers.

The angle of incidence is computed at 46 discreete angles of $\theta = 0\,^\circ$ to $\theta = 90\,^\circ$ with an increment of $\delta\theta = 2\,^\circ$. The first incidence is with $\vec{k} = -\vec{e}_x$, the last with $\vec{k} = -\vec{e}_y$. After having meshed the sphere, neither the mesh is modified, nor is the sphere rotated. This is to test the accurary of the computation when the wave is incident in different directions with respect to the vertices of the mesh. Of course, the result should not change with the incident angle.

In Fig. 10, the monostatic radar cross section is shown for the discretizations $a1$ and $a2$. The marked lines show

TABLE II
MESHING SCHEMES USED FOR THE COMPUTATIONS.

scheme	surface elements	property
a	triangular	mesh points are chosen on geometrical surface
b	triangular	mesh as a, but also includes geometrical symmetry
c	triangular	mesh as b, additionally the total surface area of triangles is scaled to match the surface area of the sphere
d	biquadratic	mesh points are chosen on geometrical surface without taking into account symmetry

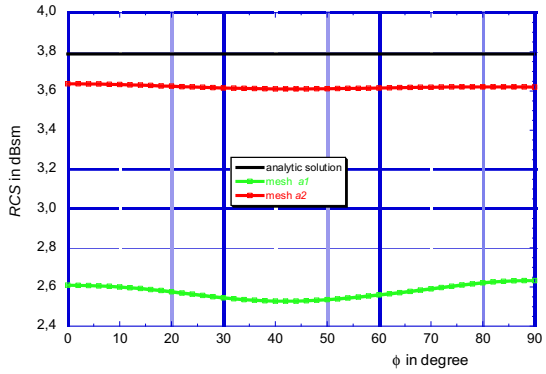

Fig. 10. Monostatic RCS of a PEC sphere computed for different angles of incidence. The sphere is meshed by 288 and 2586 linear triangles according scheme a.

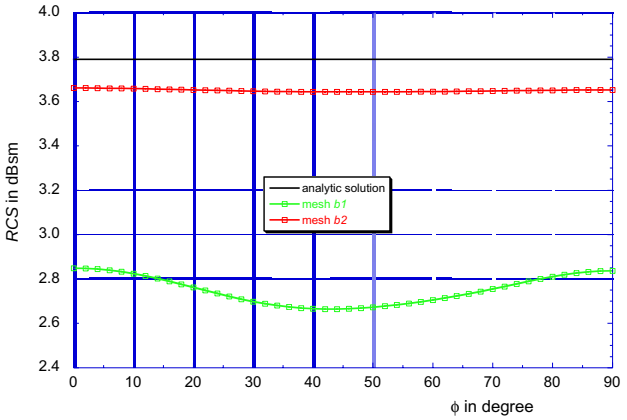

Fig. 11. Monostatic RCS of a PEC sphere computed for different angles of incidence. The sphere is meshed by 352 and 2688 linear triangles, the mesh includes the symmetry of the sphere according to scheme b.

the computed radar cross section for the two meshes. For mesh $a1$, the computed radar cross section has a minimum and maximum value of $RCS_{\min,a1} = 2.5282$ dBsm and $RCS_{\max,a1} = 2.6335$ dBsm for an average level of $RCS_{\text{ave},a1} = 2.5766$ dBsm. The amplitude $RCS_{\max,a1} - RCS_{\min,a1}$ is $\Delta RCS_{a1} = 0.105$ or 4.1 %. The absolute deviation from the analytical value is 32 %. Mesh $a2$ yields more accurate values of $RCS_{\min,a2} = 3.611$ dBsm, $RCS_{\max,a2} = 3.637$ dBsm, $RCS_{\text{ave},a2} = 3.621$ dBsm, and $\Delta RCS_{a2} = 0.026$ or 0.72 %, respectively. The absolute error to the analytical value is 4.45 %. At a frequency of $f = 150$ MHz, each triangle has a surface of at most $\lambda^2/90$.

Fig. 11 shows the results for meshes $b1$ and $b2$. For $b1$, the radar cross section has a minimum and maximum value of $RCS_{\min,b1} = 2.664$ dBsm and $RCS_{\max,b1} = 2.848$ dBsm, respectively, for an average of $RCS_{\text{ave},b1} = 2.750$ dBsm. The amplitude is $\Delta RCS_{b1} = 0.184$ or 6.7 %, the absolute deviation to the analytical value is only 27 %. Mesh $b2$ yields $RCS_{\min,b2} = 3.643$ dBsm, $RCS_{\max,b2} = 3.660$ dBsm, $RCS_{\text{ave},b2} = 3.649$ dBsm, and $\Delta RCS_{b2} = 0.018$ or 0.48 %, respectively. The absolute error compared to the analytical value is 3.7 %. In conclusion, taking the symmetry of the scatterer into account increases slightly the accuracy of the computation. Still, many triangles and, hence, unknowns are necessary to obtain results that appear acceptable.

The meshes $c1$ and $c2$ yield results that are shown in Fig. 12. They are found to be of much better agreement with the analytical value than the above results. In particular, mesh $c1$ yields in a computed radar cross section with a minimum value and a maximum value of $RCS_{\min,c1} = 3.535$ dBsm and $RCS_{\max,c1} = 3.709$ dBsm, respectively, for a mean level of $RCS_{\text{ave},c1} = 3.611$ dBsm. The difference $RCS_{\max,a1} - RCS_{\min,a1}$ is hence $\Delta RCS_{c1} = 0.174$ or 4.8 %. The absolute deviation to the analytical value is only 4.7 % indicating that the accurate representation of the actual surface of the scatterer is important. Mesh $c2$ yields slightly more accurate values of $RCS_{\min,c2} = 3.763$ dBsm, $RCS_{\max,c2} = 3.780$ dBsm, $RCS_{\text{ave},c2} = 3.769$ dBsm, and $\Delta RCS_{c2} = 0.017$ or 0.46 %, respectively. Again, the absolute error to the analytical value is 0.54 %. It is, hence, obvious from the data that an accurate geometrical approximation including symmetry and surface of the scatterer is necessary for good computational results, especially when highly accurate radar cross sections are computed.

Finally, the sphere is meshed by the biquadratic surface elements according to scheme d. The computed radar cross section, also shown in Fig. 12, is with a very good agreement with the analytical value with an error of only 1.5 %. The computed RCS has minimum and maximum values, average and error are $RCS_{\min,d} = 3.721$ dBsm, $RCS_{\max,d} = 3.743$ dBsm, $RCS_{\text{ave},d} = 3.733$ dBsm, and $\Delta RCS_d = 0.0213$ or 0.57 %, respectively. It is noted that for the triangular meshes only the one with symmetry and

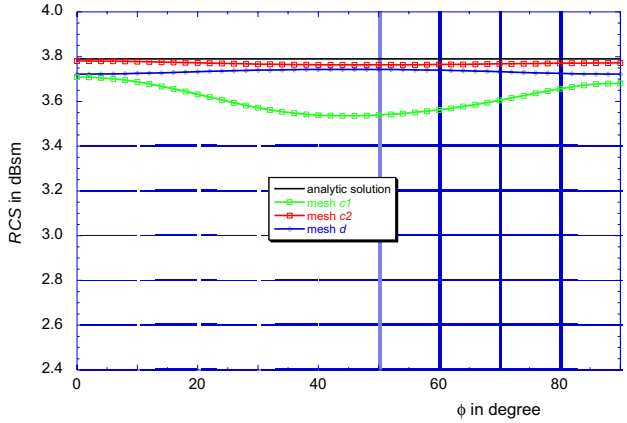

Fig. 12. Monostatic RCS of a PEC sphere computed for different angles of incidence. The sphere is meshed by 352 and 2688 linear triangles with a mesh that includes symmetry, the total surface of the triangles corresponds to the sphere's surface according to scheme c. Additionally, the sphere is meshed by a biquadratic mesh that has 216 biquadratic rectangles according to scheme d.

a geometric scaling for the actual surface yields better results, with a high cost of 4032 unknowns.

Table III concludes of the meshing schemes, the amplitudes of the computed RCS values, the average RCS-values and the errors.

D. Frequency Sweep for a PEC Sphere

Next is a frequency sweep of the above sphere for a plane wave incident with $\vec{k} = -\vec{e}_x$. The mesh is left unmodified for the frequencies from $f_\mathrm{l} = 100$ MHz to $f_\mathrm{u} = 500$ MHz. The results for meshes $c1$, $c2$ and d are reproduced. The sizes of the surface elements in terms of squared wavelengths for the frequencies $f = 300$ MHz and $f = 500$ MHz are shown in Tab. IV together with the absolute values..

Fig. 13 shows the radar cross section of the three numerical schemes in comparison with the analytical MIE solution. It is seen that the coarse mesh $c1$ yields, over the complete frequency range, results that do not correspond well to the analytical values. The fine mesh $c2$ with 4032 unknowns results in radar cross section values that are still far away from the analytical solution, but better than the smaller mesh for frequencies of up to $f \approx 250$ MHz. Starting from $f \approx 300$ MHz, the two curves deviate from each other. The triangular mesh shows erroneous results at frequencies around $f \approx 390$ MHz which is close to the inner resonance frequency $p = 1, m = 4$ of the sphere. The mesh with the biquadratic quadrangles is on the analytical curve for frequencies up to $f \approx 500$ MHz.

The mesh using triangular discretization cells yields accurate results only for cell sizes areas that are smaller than $\lambda^2/90$. In contrast, the biquadratic quadrangles yield still accurate results for large cells comparable to $\lambda^2/10$. Hence, less cells can be used to discretize a scatterer resulting in smaller problem sizes with higher accuracy.

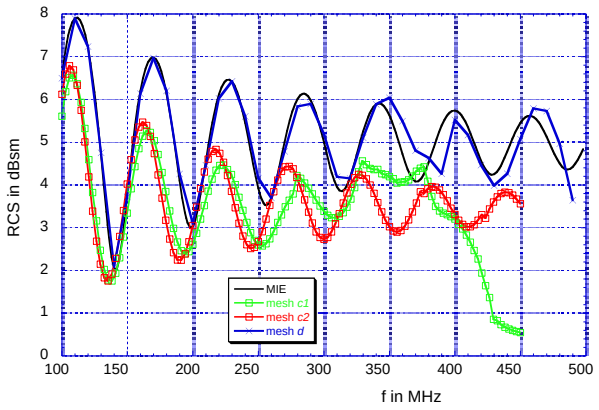

Fig. 13. RCS of a perfect conducting sphere. Triangular mesh with 352 and 2688 elements in comparison with 216 biquadratic quadrangles and the theoretical values.

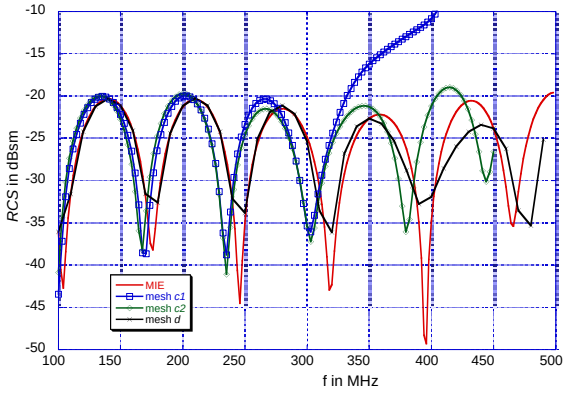

Fig. 14. RCS of a sphere with a low dielectric contrast, $\varepsilon_r = 1.1$.

E. Frequency Sweep for a Low Contrast Sphere

With the same meshes as previously, the radar cross section of a dielectric sphere with a very low contrast of $\varepsilon_r = 1.1$ is computed. This case is especially difficult to model numerically as the contrast is very low.

Mesh $c1$ and $c2$ yield both results that are not accurately modelling the zeros of the frequency response. The average level still corresponds to the average level of the analytic Mie results. Mesh $c1$ yields completely wrong results starting at 300 MHz, whereas mesh $c2$ somewhat follows the analytic values up to a frequency of 400 MHz.

Mesh d together with the complete PMCHW formulation yields the results in Fig. 14 compared to the analytic results. The numerical solution follows the analytic solution up to a frequency of about 350 MHz.

V. Conclusions

For accurate numerical solutions by boundary element methods applied to scattering problems, two main issues should be considered carefully: the geometrical approximation of the surface of the scatterer and the numerical approximation of the physical quantity on the boundary.

TABLE III

AMPLITUDE AND AVERAGE RCS COMPUTED BY THE MESHING SCHEMES IDENTIFIED IN TABLE II FOR A SPHERE OF RADIUS 1 m. ANALYTICAL VALUE IS $RCS_{\mathrm{MIE}} = 3.789$ dBsm.

Mesh	# unknowns	Amplitude ΔRCS/dBsm	Average RCS_{ave}/dBsm	error in %
$a1$	432	0.105	2.58	32
$a2$	3879	0.026	3.62	4.5
$b1$	528	0.184	2.75	27
$b2$	4032	0.018	3.49	3.7
$c1$	528	0.174	3.61	4.7
$c2$	4032	0.017	3.77	0.5
d	432	0.021	3.73	1.5

TABLE IV

AVERAGE DISCRTIZATION CELL SIZES NORMALIZED TO SQUARED WAVELENGTH FOR THE THREE MESHING SCHEMES.

scheme	type	no. of cells	average size in m^2	$f = 300$ MHz	$f = 500$ MHz
$c1$	triangular	352	$a_{\mathrm{c1}} = 38.7 \cdot 10^{-3}$	$\lambda^2/26$	$\lambda^2/9$
$c2$	triangular	2688	$a_{\mathrm{c2}} = 5.14 \cdot 10^{-3}$	$\lambda^2/194$	$\lambda^2/70$
d	biquadratic	216	$a_{\mathrm{d}} = 58.2 \cdot 10^{-3}$	$\lambda^2/34$	$\lambda^2/6$

Utilizing linear triangles has the advantage of simple meshing algorithms, the ability to model almost any surface and the relatively simple mathematical formulation. The limits of the linear triangles show up when currents close to edges or borders must be computed: a non-physical solution may result. Also, as it is necessary to mesh the geometrical surface area as close as possible by the approximation, accurate results may only be obtained when the surface area of the numerical model is scaled to match the surface area of the physical problem.

Biquadratic quadrangles are somewhat more difficult to be described mathematically. They need more surface points for discretization, but yield a much more accurate description of the physical problem. This results in fewer surface elements and consequently less unknowns in the numerical formulation. The present contribution also has shown that a formulation founded on biquadratic quadrangles may use considerably larger elements compared to a formulation based on linear triangles with the same numerical accuracy.

REFERENCES

[1] R. F. Harrington, *Field Computation by Moment Methods*. New York: The Macmillan Company, 1968.

[2] A. J. Poggio and E. K. Miller, "Integral equation solutions of three-dimensional scattering problems," in *Computer Techniques for Electromagnetics* (R. Mittra, ed.), New York, NY, USA: Pergamon Press, 1973.

[3] A. Herschlein, *Entwicklung numerischer Verfahren zur Feldberechnung konformer Antennen auf Oberflächen höherer Ordnung* (in German). PhD thesis, Institut für Höchstfrequenztechnik und Elektronik, Universität Karlsruhe, 2002.

[4] A. Herschlein, J. von Hagen, and W. Wiesbeck, "A generalized integral equation formulation for mixed-dielectric-PEC-scatterers," *Radio Science*, vol. 37, no. 4, pp. 11–1 – 11–15, 2002.

[5] S. M. Rao, D. R. Wilton, and A. W. Glisson, "Electromagnetic scattering from surfaces of arbitrary shape," *IEEE Trans. on Ant. and Prop.*, vol. 30, pp. 409–418, May 1982.

[6] G. Kang, J. Song, W. C. Chew, K. C. Donepudi, and J.-M. Jin, "A novel grid-robust higher order vector basis function for the method of moments," *IEEE Trans. on Ant. and Prop.*, vol. 49, pp. 908–915, June 2001.

[7] J. M. Song and W. C. Chew, "Moment method solutions using parametric geometry," *J of Electromagnetic Waves and Applications*, pp. 71–83, Jan. 1995.

[8] J. Dominguez, *Boundary Elements in Dynamics*. London: Computational Mechanics Publications, Elsevier Applied Science, 1993.

[9] A. Herschlein, J. von Hagen, and W. Wiesbeck, "Methods for the evaluation of regular, weakly singular and strongly singular surface reaction integrals arising in method of moments," *ACES Journal*, vol. 17, *Special Issue on: Approaches on better Accuracy/Resolution in CEM*, pp. 63–73, Mar. 2002.

[10] G. Mie, "Beiträge zur Optik trüber Medien, speziell kolloidaler Metalllösungen," *Annalen der Physik*, vol. 4, no. 25, 1908.

Alexander Herschlein received the Dipl.-Ing. (M.S.E.E.) and the Dr.-Ing. (Ph.D.E.E.) degrees from the University of Karlsruhe, Germany, in 1993 and 2002, respectively. F rom 1994 to 2002, he was with the Institut für Höchstfrequenztechnik und Elektronik (IHE), University of Karlsruhe. As a research assistant at the IHE, he was responsible for lectures in antennas and antenna systems. His research responsibilities during this period included field theory, numerical methods, optimisations, wave propagation, antennas and EMC. 1998 and 1999, he also worked for the DaimlerChrysler AG, Research Center Ulm, Germany.

Since 2003, he has been with EADS-Astrium in Friedrichshafen, Germany, engaged in microwave system engineering. He is the head of the antenna laboratory, responsible for antenna designs and optimisations, RF test definitions and RF measurements. His main topic is the optimisation of the active TerraSAR-X antenna and he is the leader of the measurement campaign of this phased array.

Jürgen v. Hagen received the Dipl.-Ing. (M.S.E.E) and the Dr.-Ing. (Ph.D.E.E.) degrees from the University of Karlsruhe (TH) in 1994 and 1997, respectively. From 1994 to 1997 he was working with the CNRS (Comité National de la Recherche Scientifique), France on electromagnetic compatibility. In 1998 he held a postdoctoral position at the Electromagnetics Research Laboratory at the Pennsylvania State University, in State College, PA, USA. 1999 until 2001 he was with the Institut für Höchstfrequenztechnik und Elektronik (IHE) at the Universität Karlsruhe (TH), Germany where he was lecturer responsible for planar and conformal antennas as well as numerical techniques in electromagnetics and research assistant for industrial applications of microwaves, microwave heating processes, and EMC. He is now with DaimlerChrysler AG, Sindelfingen, responsible for broadcast reception systems, and continues to teach microstrip and planar antennas at the University of Karlsruhe.

His research interests other than his current professional area are electromagnetic theory, numerical techniques including frequency and time domain techniques, planar and conformal antennas, industrial applications of microwave power, and automotive sensors.

Dr. v. Hagen is member of IEEE, ACES, and VDE.

Dietmar Löffler received the Dipl.-Ing. (M.S.E.E.) and the Dr.-Ing. (Ph.D. E.E.) degrees from the University of Karlsruhe (TH), Germany in 1995 and 2001, respectively. From 1995 to 2001 he was working with the Institut für Höchstfrequenztechnik und Elektronik (IHE) at the University of Karlsruhe, Germany on wave propagation, microstrip circuits and conformal antennas used for radar and communication applications. For the Carl-Cranz-Gesellschaft (CCG), Germany, he served as a lecturer of the courses "Radar System Engineering" and "Smart Antennas".

In 2001 he joined the LS Telcom AG, Lichtenau, Germany, where he currently is the head of the broadcasting department. His research interests are digital broadcast systems in the short wave range, digital television system in the VHF/UHF bands as well as wave propagation within the broadcasting bands.

Dr. Löffler is a member of VDE.

Werner Wiesbeck received the Dipl.-Ing. (M.S.E.E.) and the Dr.-Ing. (Ph.D.E.E.) degrees from the Technical University Munich in 1969 and 1972, respectively. From 1972 to 1983 he was with AEG-Telefunken in various positions including that of head of R&D of the Microwave Division in Flensburg and marketing director Receiver and Direction Finder Division, Ulm. During this period he had product responsibility for mm-wave radars, receivers, direction finders and electronic warfare systems. Since 1983 he has been director of the Institut für Höchstfrequenztechnik und Elektronik (IHE) at the University of Karlsruhe (TH), where he had been dean of the Faculty of Electrical Engineering. Research topics include radar, remote sensing, wireless communication and antennas. In 1989 and 1994, respectively, he spent a six month sabbatical at the Jet Propulsion Laboratory, Pasadena. He is a member of the IEEE GRS-S AdCom (1992 - 2000), Chairman of the GRS-S Awards Committee (1994 - 1998, 2002 -), Executive Vice President IEEE GRS-S (1998 - 1999), President IEEE GRS-S (2000 - 2001), Associate Editor IEEE-AP Transactions (1996-1999), past and present Treasurer of the IEEE German Section (1987-1996, 2003-2005). He has been General Chairman of the '88 Heinrich Hertz Centennial Symposium, the '93 Conference on Microwaves and Optics (MIOP '93), the Technical Chairman of International mm-Wave and Infrared Conference 2004 and he has been a member of the scientific committees of many conferences. For the Carl Cranz Series for Scientific Education he serves as a permanent lecturer for radar system engineering, wave propagation and mobile communication network planning. He is a member of an Advisory Committee of the EU - Joint Research Centre (Ispra/Italy), and he is an advisor to the German Research Council (DFG), to the Federal German Ministry for Research (BMBF), and to industry in Germany. He is recipient of a number of awards, lately the IEEE Millennium Award, and the IEEE GRS Distinguished Achievement Award. He is a Fellow of IEEE, a Member of the Heidelberger Academy of Sciences and a Member of acatech (German Academy of Engineering and Technology).